Research Article | Vol. 24, No. 24 | 28 Nov 2016 | OPTICS EXPRESS 27890

Optics EXPRESS

Antiresonant reflecting guidance mechanism in hollow-core fiber for gas pressure sensing

MAOXIANG HOU,[1,2] FENG ZHU,[2] YING WANG,[2,4] YIPING WANG,[2,5] CHANGRUI LIAO,[2] SHEN LIU,[2] AND PEIXIANG LU[1,3]

[1]*Wuhan National Laboratory for Optoelectronics and School of Physics, Huazhong University of Science & Technology, Wuhan 430074, China*
[2]*Key Laboratory of Optoelectronic Devices and Systems of Ministry of Education/Guangdong Province, Shenzhen University, Shenzhen 518060, China*
[3]*Laboratory of Optical Information Technology, Wuhan Institute of Technology, Wuhan 430205, China*
[4]*yingwang@szu.edu.cn*
[5]*ypwang@szu.edu.cn*

Abstract: A gas pressure sensor based on an antiresonant reflecting guidance mechanism in a hollow-core fiber (HCF) with an open microchannel is experimentally demonstrated for gas pressure sensing. The microchannel was created on the ring cladding of the HCF by femtosecond laser drilling to provide an air-core pressure equivalent to the external environment. The HCF cladding functions as an antiresonant reflecting waveguide, which induces sharp periodic lossy dips in the transmission spectrum. The proposed sensor exhibits a high pressure sensitivity of 3.592 nm/MPa and a low temperature cross-sensitivity of 7.5 kPa/°C. Theoretical analysis indicates that the observed high gas pressure sensitivity originates from the pressure induced refractive index change of the air in the hollow-core. The good operation durability and fabrication simplicity make the device an attractive candidate for reliable and highly sensitive gas pressure measurement in harsh environments.

OCIS codes: (060.2270) Fiber characterization; (140.3948) Microcavity devices; (060.2370) Fiber optics sensors.

References and links

1. Y. J. Rao, "Recent progress in fiber-optic extrinsic Fabry–Pérot interferometric sensors," Opt. Fiber Technol. **12**(3), 227–237 (2006).
2. Q. Zhang, N. Liu, T. Fink, H. Li, W. Peng, and M. Han, "Fiber-optic pressure sensor based on-phase-shifted fiber Bragg grating on side-hole fiber," IEEE Photonics Technol. Lett. **24**(17), 1519–1522 (2012).
3. J. Tang, G. Yin, S. Liu, X. Zhong, C. Liao, Z. Li, Q. Wang, J. Zhao, K. Yang, and Y. Wang, "Gas pressure sensor based on CO_2-Laser-Induced Long-Period fiber grating in Air-Core photonic bandgap fiber," IEEE Photon. J. **7**(5), 1–7 (2015).
4. X. Zhong, Y. Wang, C. Liao, S. Liu, J. Tang, and Q. Wang, "Temperature-insensitivity gas pressure sensor based on inflated long period fiber grating inscribed in photonic crystal fiber," Opt. Lett. **40**(8), 1791–1794 (2015).
5. Z. Liu, M. L. V. Tse, C. Wu, D. Chen, C. Lu, and H. Y. Tam, "Intermodal coupling of supermodes in a twin-core photonic crystal fiber and its application as a pressure sensor," Opt. Express **20**(19), 21749–21757 (2012).
6. Z. Li, C. Liao, Y. Wang, L. Xu, D. Wang, X. Dong, S. Liu, Q. Wang, K. Yang, and J. Zhou, "Highly-sensitive gas pressure sensor using twin-core fiber based in-line Mach-Zehnder interferometer," Opt. Express **23**(5), 6673–6678 (2015).
7. W. Talataisong, D. N. Wang, R. Chitaree, C. R. Liao, and C. Wang, "Fiber in-line Mach-Zehnder interferometer based on an inner air-cavity for high-pressure sensing," Opt. Lett. **40**(7), 1220–1222 (2015).
8. H. Y. Fu, H. Y. Tam, L.-Y. Shao, X. Dong, P. K. A. Wai, C. Lu, and S. K. Khijwania, "Pressure sensor realized with polarization-maintaining photonic crystal fiber-based Sagnac interferometer," Appl. Opt. **47**(15), 2835–2839 (2008).
9. L. Jin, B. Guan, and H. Wei, "Sensitivity characteristics of Fabry–Pérot pressure sensors based on hollow-core microstructured fibers," J. Lightwave Technol. **31**(15), 2526–2532 (2013).
10. Y. Wang, D. N. Wang, C. Wang, and T. Hu, "Compressible fiber optic micro-Fabry-Pérot cavity with ultra-high pressure sensitivity," Opt. Express **21**(12), 14084–14089 (2013).
11. C. Liao, S. Liu, L. Xu, C. Wang, Y. Wang, Z. Li, Q. Wang, and D. N. Wang, "Sub-micron silica diaphragm-based fiber-tip Fabry-Perot interferometer for pressure measurement," Opt. Lett. **39**(10), 2827–2830 (2014).
12. J. Ma, W. Jin, H. L. Ho, and J. Y. Dai, "High-sensitivity fiber-tip pressure sensor with graphene diaphragm," Opt. Lett. **37**(13), 2493–2495 (2012).

#273733 http://dx.doi.org/10.1364/OE.24.027890
Journal © 2016 Received 12 Aug 2016; revised 8 Oct 2016; accepted 9 Nov 2016; published 21 Nov 2016

Optics EXPRESS

13. F. Xu, D. Ren, X. Shi, C. Li, W. Lu, L. Lu, L. Lu, and B. Yu, "High-sensitivity Fabry-Perot interferometric pressure sensor based on a nanothick silver diaphragm," Opt. Lett. **37**(2), 133–135 (2012).
14. M. Hou, Y. Wang, S. Liu, J. Guo, Z. Li, and P. Lu, "Sensitivity-Enhanced pressure sensor with Hollow-Core photonic crystal fiber," J. Lightwave Technol. **32**(3), 4035–4039 (2014).
15. N. M. Litchinitser, A. K. Abeeluck, C. Headley, and B. J. Eggleton, "Antiresonant reflecting photonic crystal optical waveguides," Opt. Lett. **27**(18), 1592–1594 (2002).
16. N. M. Litchinitser, S. C. Dunn, B. Usner, B. J. Eggleton, T. P. White, R. C. McPhedran, and C. M. de Sterke, "Resonances in microstructured optical waveguides," Opt. Express **11**(10), 1243–1251 (2003).
17. P. Rugeland, C. Sterner, and W. Margulis, "Visible light guidance in silica capillaries by antiresonant reflection," Opt. Express **21**(24), 29217–29222 (2013).
18. C. H. Lai, B. You, J. Y. Lu, T. A. Liu, J. L. Peng, C. K. Sun, and H. C. Chang, "Modal characteristics of antiresonant reflecting pipe waveguides for terahertz waveguiding," Opt. Express **18**(1), 309–322 (2010).
19. G. J. Pearce, G. S. Wiederhecker, C. G. Poulton, S. Burger, and J. Russell, "Models for guidance in kagome-structured hollow-core photonic crystal fibres," Opt. Express **15**(20), 12680–12685 (2007).
20. S. Liu, N. Liu, M. Hou, J. Guo, Z. Li, and P. Lu, "Direction-independent fiber inclinometer based on simplified hollow core photonic crystal fiber," Opt. Lett. **38**(4), 449–451 (2013).
21. W. Belardi and J. C. Knight, "Effect of core boundary curvature on the confinement losses of hollow antiresonant fibers," Opt. Express **21**(19), 21912–21917 (2013).
22. A. M. Zheltikov, "Ray-optic analysis of the (bio)sensing ability of ring-cladding hollow waveguides," Appl. Opt. **47**(3), 474–479 (2008).
23. R. Gao, Y. Jiang, and Y. Zhao, "Magnetic field sensor based on anti-resonant reflecting guidance in the magnetic gel-coated hollow core fiber," Opt. Lett. **39**(21), 6293–6296 (2014).
24. R. Gao, D. Lu, J. Cheng, Y. Jiang, L. Jiang, and Z. Qi, "Humidity sensor based on power leakage at resonance wavelengths of a hollow core fiber coated with reduced graphene oxide," Sens. Actuat. Biol. Chem. **222**, 618–624 (2016).
25. Y. Wang, C. R. Liao, and D. N. Wang, "Femtosecond laser-assisted selective infiltration of microstructured optical fibers," Opt. Express **18**(17), 18056–18060 (2010).
26. S. Liu, Y. Wang, M. Hou, J. Guo, Z. Li, and P. Lu, "Anti-resonant reflecting guidance in alcohol-filled hollow core photonic crystal fiber for sensing applications," Opt. Express **21**(25), 31690–31697 (2013).
27. R. Gao, D. F. Lu, J. Cheng, Y. Jiang, L. Jiang, and Z. M. Qi, "Optical displacement sensor in a capillary covered hollow core fiber based on anti-resonant reflecting guidance," IEEE J. Sel. Top. Quantum Electron. **23**(2), 5600106 (2017).
28. K. P. Birch and M. J. Downs, "An updated Edlen equation for the refractive index of air," Metrologia **30**(3), 155–162 (1993).
29. W. D. Pilkey, *Peterson's Stress Concentraton Factors* 2nd ed. (NY, USA: Wiley, 1999).
30. M. Pang, H. F. Xuan, J. Ju, and W. Jin, "Influence of strain and pressure to the effective refractive index of the fundamental mode of hollow-core photonic bandgap fibers," Opt. Express **18**(13), 14041–14055 (2010).
31. Y. Cao, W. Jin, F. Yang, and H. L. Ho, "Phase sensitivity of fundamental mode of hollow-core photonic bandgap fiber to internal gas pressure," Opt. Express **22**(11), 13190–13201 (2014).
32. A. Michie, J. Canning, K. Lyytikäinen, M. Aslund, and J. Digweed, "Temperature independent highly birefringent photonic crystal fibre," Opt. Express **12**(21), 5160–5165 (2004).

1. Introduction

Gas pressure sensing is one of the most important applications of fiber optic devices in industrial and environmental monitoring fields [1]. In the past decades, various optical fiber configurations, such as fiber gratings [2–4], Mach-Zehnder interferometers (MZIs) [5–7], Sagnac interferometers (SIs) [8] and Fabry-Pérot interferometers (FPIs) [9–14] have been developed for pressure sensing applications. Pressure sensors based on fiber gratings generally present low sensitivities on the order of 0.01 nm/MPa [2,3]. While an inflated long-period fiber grating (LPFG) has been demonstrated with an improved sensitivity of 1.68 nm/MPa [4]. MZI and SI based sensors usually require precise manufacturing operation, and relatively complex structures, which limit their mass production and practical applications [5–8]. Fiber-tip FPIs based on various diaphragm materials have shown good potential for pressure sensing applications, however, the durability and operation stability of the devices may be limited by the thin diaphragm structure [12–14].

Antiresonant reflecting fiber is a kind of waveguide that spectral characteristics are governed by the thickness of the first high-index layer rather than lattice constant, and has been identified to play an important role in near-infrared and THz optical signal transmission [15–18]. Various structures of antiresonant reflecting fibers have been reported, including photonic crystal fibers (PCFs) [15,16], Kagome fibers [19,20], "negative curvature" fiber [21]

Optics EXPRESS

and the simplest structure of ring-cladding hollow-core fiber (HCF) [22]. Moreover, HCF coated with functional material films have been reported for biosensing, magnetic field sensing and humidity sensing [22–24].

In this letter, we present a gas pressure sensor based on an antiresonant reflecting guidance (ARRG) mechanism in an HCF. The pressure sensor is comprised of an HCF section with an open microchannel fabricated through the ring cladding of the HCF by femtosecond (fs) laser micromachining [25]. Here, the HCF serves as an antiresonant reflecting waveguide, and the microchannel allows for an air-core pressure equivalent to that of the external pressure. The ARRG-based sensor exhibits sharp periodic lossy dips in the transmission spectrum, and the resonant lossy dips exhibit a wavelength shift with a linear sensitivity of 3.59 nm/MPa and a low temperature cross-sensitivity of 7.5 kPa/°C. Theoretical analyses indicate that the pressure sensitivities for the ARRG sensors mainly result from the refractive index change of air within the hollow-core. Moreover, the proposed device exhibits the advantage of novelty, simplicity and high sensitivity.

2. Fabrication

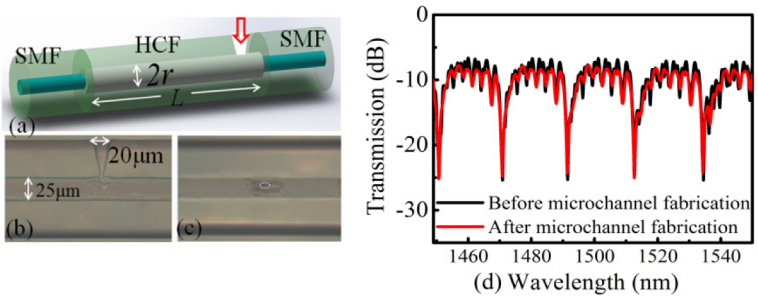

Fig. 1. (a) Pictorial view of the designed pressure sensor based on an antiresonant reflecting guidance (ARRG) mechanism in a hollow-core fiber (HCF). (b) Side-view and (c) top-view optical microscopy images of the microchannel created by femtosecond laser micromachining. (d) Transmission spectra of the ARRG-based pressure sensor with an HCF length of 5 mm before and after microchannel fabrication.

Figure 1(a) shows a pictorial illustration of the designed open ARRG-based pressure sensor, comprised of an HCF section of length (L) spliced between two single-mode fiber (SMF) sections and with a microchnnel passing through the ring cladding of the HCF in a direction perpendicular to its core. The HCF employed in the experiments (Polymicro Technologies, TSP025150) consisted of a 25 μm diameter ($2r$) of and a ring-cladding with a thickness (d) of 50 μm. The HCF section was spliced to the SMFs using a Fujikura 80S fusion splicer.

In the fs laser micromachining process employed for micro-channel fabrication, 800 nm wavelength fs laser pulses with duration of 120 fs and pulse energy of 2 μJ at a repetition rate of 1 kHz were focused onto the outside surface of the HCF through a 20 × microscope objective lens. The initially closed sensor specimen was fixed to a linear translation stage, and the laser beam was initially scanned parallel to the fiber axis at a speed of 2 μm/s over a total distance of 20 μm. After one scanning cycle, the laser beam focus point was shifted 10 μm perpendicular to the fiber axis, for the next scanning cycle. After four scanning cycles, a V shaped microchannel was successfully fabricated in the cladding of the HCF, which allows for an air-core pressure equivalent to that of the external pressure, as shown in Figs. 1(b) and 1(c).

Figure 1(d) shows the transmission spectra of an L = 5 mm specimen before and after microchannel fabrication. The transmission spectra of the sample were collected with a broadband light source (BBS; Shenzhen Fiberlaker Technology Co., Ltd.) ranging from 1250 to 1650 nm and an optical spectrum analyzer (OSA; Yokogawa AQ6370C) with a resolution of 0.02 nm. Prior to microchannel fabrication, the initial insertion loss was approximately –7

Optics EXPRESS

dB, which mainly derived from the transmission loss of the HCF. After microchannel fabrication, the insertion loss increased to approximately −8 dB, and the resonance wavelengths remained unchanged. Five sharp resonance lossy dips were observed in the 100 nm wavelength range shown in Fig. 1(d).

3. Guiding mechanism

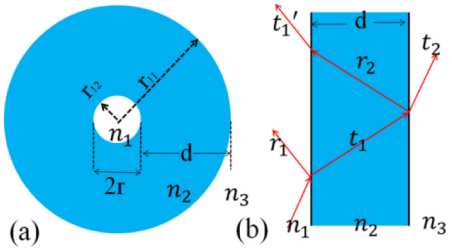

Fig. 2. (a) Schematic diagram of an HCF cross section with cladding of thickness d and index of refraction n_2. The indices of refraction of the hollow core and external environment are n_1 and n_3, respectively. (b) The optical pathways at the HCF interfaces.

To explain the data presented in Fig. 1(d), a schematic diagram of the HCF cross-section is shown in Fig. 2(a). The air-core has an index of refraction n_1 and the ring cladding has an index of refraction n_2. Air also resides external to the cladding, and has an index of refraction n_3 that is dependent on the external pressure. The optical guidance mechanism of the HCF can be explained according to the antiresonant reflecting optical waveguide (ARROW) model. In this model, the high refractive index cladding is regarded as a Fabry-Pérot etalon. Figure 2(b) illustrates multiple beams at the interfaces within the FP-etalon. The light intensity corresponding to the resonant condition can be easily interpreted by referring to geometrical optics. In the ARROW model, light passes out of the high refractive index cladding when its wavelengths is close to that of a resonant wavelength λ_m, which results in the sharp periodic lossy dips in the transmission spectrum shown in Fig. 1(d). However, when the propagating wavelength is far away from a resonant wavelength (i.e. the antiresonant wavelengths region), the light is internally reflected, confined in the hollow core of the fiber as the guided core mode. The resonant wavelengths λ_m can be expressed as follows [15]:

$$\lambda_m = \frac{2d}{m}\sqrt{n_2^2 - n_1^2} \tag{1}$$

where m is an integer beginning with 1, $d = 50$ μm and $n_2 = 1.4446$ (around 1500 nm) and $n_1 = 1$ (under normal pressure).

By using the commercial COMSOL software, the transmission spectrum of the HCF was simulated with full-vector finite element method (FEM) [23], as shown in Fig. 3(a). Given that the guided light is assumed as a Gaussian beam with a diameter of 9 μm. The theoretical resonant wavelengths were calculated as 1499.51 nm and 1520.64 nm, around 1500 nm.

Moreover, Fig. 3(a) also presents the transmission spectra of three sensor specimens with L values of 1.5, 2, and 5 mm, where the locations of the sharp transmission lossy dips for the three samples exhibit slight deviations with the theoretical predictions. This might be related to the thickness of the silica cladding d, which is not very strictly uniform at different positions of the HCF. The transmission lossy dips of the three samples are –3.5, –4.8, and –7 dB, respectively, result from incomplete confine of light by the single layer ring cladding structure of HCF [16]. The visibilities of the three samples are 4.4, 7.5, and 17.1 dB, respectively, which indicate that the resonant effect is accumulated along the length of the HCF at resonant wavelengths [26]. Therefore, there is a tradeoff between the visibilities and the transmission lossy dips. It is noted that the transmission spectra are not particularly uniform but appear to include other periodic components, distributed throughout the

Optics EXPRESS

antiresonance regions of the transmission spectra. We believe that the guide light is also reflected on the outer surface of the HCF, but the reflectivity is relative low, which results in the ripples in the transmission spectra [27].

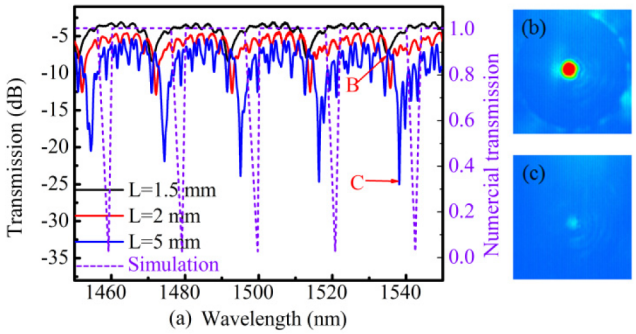

Fig. 3. (a) Simulation and measured transmission spectra. (b) and (c) Intensity distributions of near-mode field patterns corresponding to the wavelengths of 1535.8 and 1538.08 nm for the specimen with an HCF length of 5 mm.

Figures 3(b) and 3(c) present the intensity distributions of near-mode field patterns observed at the wavelength of 1535.8 and 1538.08 nm for the L = 5 mm sensor. These wavelengths respectively correspond to an antiresonance peak and main resonance loss. Figure 3(b) shows the mode field for the antiresonant wavelength, which is confined in the hollow core of the fiber as the guided core mode. Figure 3(c) shows the mode field for the resonant wavelength, and the guided light would transmit out of the HCF section and completely lost. Therefore, the HCF can be described as an ARROW.

4. Gas pressure experiments and discussion

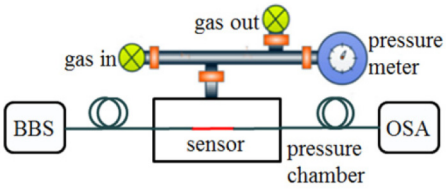

Fig. 4. Experiment setup for gas pressure measurements employing a broadband light source ranging from 1250 to 1650 nm and an optical spectrum analyzer.

The gas pressure responses of the ARRG-based sensors were tested by means of the experimental setup shown in Fig. 4. Sensors were fixed into a pressure chamber, where a commercial gas pressure generator (ConST-168) with a stability of ± 0.2 kPa and a high precision digital pressure meter (ConST-211) were employed to regulate the pressure in the chamber. The applied gas pressure in the chamber was increased from 0 to 2 MPa in interval of 0.1 MPa at room temperature, and the pressure was maintained for 5 min at each step.

The resonance wavelengths of two ARRG-based sensors with L of 5 and 2 mm gas pressures are shown in Figs. 5(a) and 5(c), respectively. The resonance transmission lossy dips of the sensors shift toward shorter wavelengths with increasing applied pressure, while the loss intensities exhibit no significant deviations, as a function of pressure. From Figs. 5(b) and 5(d), the two sensors with L = 5 mm and L = 2 mm both exhibit good linear wavelength responses with similar sensitivities of −3.592 nm/MPa and −3.585 nm/MPa, respectively. Compared with previously reported optical fiber pressure sensors, such as the inflated LPG (1.68 nm/MPa) [4], dual-core PCF (21 pm/MPa) [5], and optical fiber tip micro-bubble (1.036 nm/MPa) [11], the ~3.592 nm/MPa sensitivity of the proposed ARRG-based pressure sensor is much greater.

Optics EXPRESS

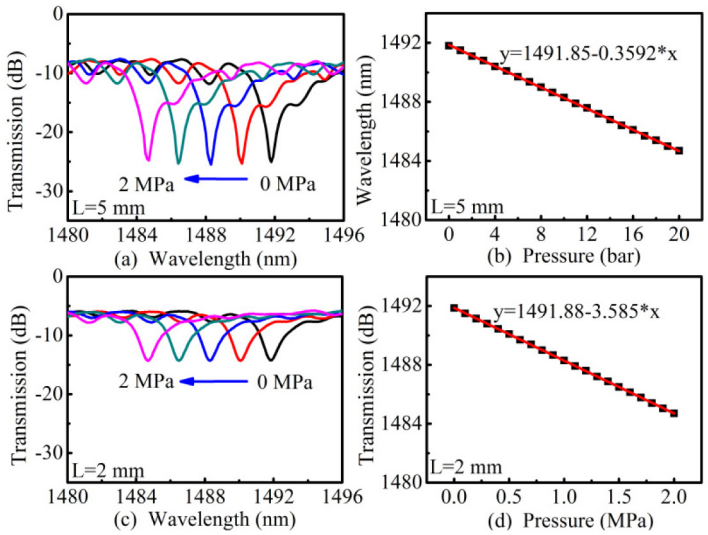

Fig. 5. Transmission spectra evolution of the opened cavity sensors (a) $L_2 = 5$ mm and (c) $L_2 = 2$ mm while the gas pressure increases from 0 to 2 MPa. Measured resonant wavelength of the two sensors (b) $L_2 = 5$ mm and (d) $L_2 = 2$ mm versus gas pressure.

For an opened ARRG-based sensor, the pressure sensitivity may be attributed to three factors: (i) refractive index change of air within the hollow-core S_{air}, (ii) structural deformation of the silica cladding $S_{structure}$, and (iii) refractive index change of silica cladding due to strain-optic effect S_{silica}. The pressure sensitivity $\partial \lambda_m/\partial P$ can be derived from Eq. (1) as

$$\frac{\partial \lambda_m}{\partial P} = S_{air} + S_{structure} + S_{silica} = -\frac{2dn_1}{m\sqrt{n_2^2 - n_1^2}} \cdot \frac{\partial n_1}{\partial P} + \frac{2\sqrt{n_2^2 - n_1^2}}{m} \cdot \frac{\partial d}{\partial P} + \frac{2dn_2}{m\sqrt{n_2^2 - n_1^2}} \cdot \frac{\partial n_2}{\partial P} \cdot \quad (2)$$

Firstly, we concern the contribution from the refractive index change of air. From an updated Edlén equation, at room temperature (15-25 °C), the index of refraction of air is a function of the pressure and temperature T (°C) [28]:

$$n_3 = n_1 = 1 + \frac{2.8793 * 10^{-9} * P}{1 + 0.003671 * T}. \quad (3)$$

As such, if the temperature remains unchanged, a linear relationship exists between n_1 and P. For T = 25°C, the pressure sensitivity S_{air} can be calculated to be approximately –3.398 nm/MPa at 1500 nm. This value is very close to the experimental results (–3.592, –3.585 nm/MPa), indicating that the air-index change played a major role in the observed pressure sensitivity.

To estimate the magnitude of $S_{structure}$ and S_{silica}, the structural deformation and strain distributions over the silica cladding region, need to be evaluated. The elasticity of HCF can be analyzed with a single-layer model with outer and inner radii r_{11} and r_{12} [9]. The stress expression in silica cladding regions can be written as [29]:

Optics EXPRESS

$$\begin{cases} \sigma_r = \dfrac{\mathrm{A}}{\mathrm{r}^2} + 2\mathrm{C} \\ \sigma_\theta = -\dfrac{\mathrm{A}}{\mathrm{r}^2} + 2\mathrm{C}, \\ \sigma_z = D \end{cases} \tag{4}$$

where A, C and D are constants. By substituting the above equations into the Hooke's law, we obtain the strain tensor for the silica cladding as [30]:

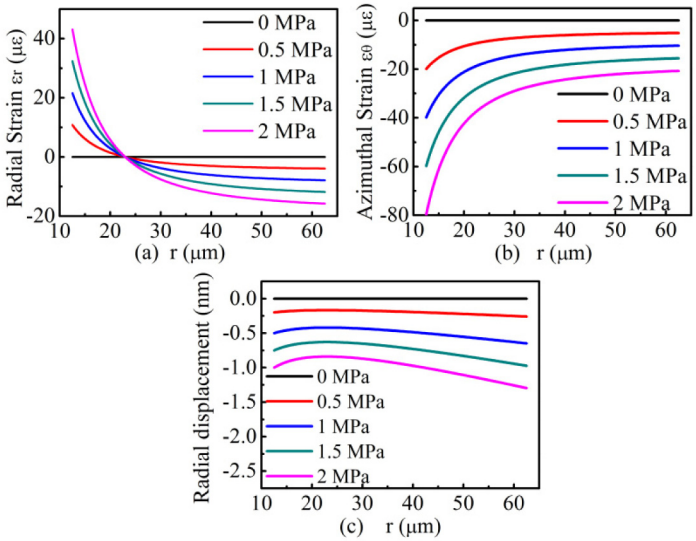

Fig. 6. Distribution of (a) radial strain, (b) azimuthal strain and (c) radial displacement of HCF for different pressures applied.

$$\begin{cases} \varepsilon_r = \dfrac{1}{\mathrm{E_{si}}}[\sigma_r - v_{si}(\sigma_r + \sigma_r)] = \dfrac{1}{\mathrm{E_{si}}}[(1+v_{si})\dfrac{A}{r^2} + 2C(1-v_{si}) - v_{si}D] \\ \varepsilon_\theta = \dfrac{1}{\mathrm{E_{si}}}[\sigma_\theta - v_{si}(\sigma_r + \sigma_z)] = \dfrac{1}{\mathrm{E_{si}}}[-(1+v_{si})\dfrac{A}{r^2} + 2C(1-v_{si}) - v_{si}D]. \\ \varepsilon_z = \dfrac{1}{\mathrm{E_{si}}}[\sigma_z - v_{si}(\sigma_r + \sigma_\theta)] = \dfrac{1}{\mathrm{E_{si}}}[D - 4v_{si}C] \end{cases} \tag{5}$$

Considering the situation of the opened ARRG sensor, the boundary conditions may be written as:

$$\begin{cases} \sigma_{r=r11} = -\mathrm{P} \\ \sigma_{r=r12} = \mathrm{P} \\ \pi\sigma_z(r_{11}^2 - r_{12}^2) + P\pi r_{11}^2 = 0 \end{cases}. \tag{6}$$

Since the sensor is fixed in the chamber, the pressure applied from the two ends would have little or no effect on its length, the pressure-induced longitudinal strain εz is also negligible [31]. With Eqs. (4)–Eqs. (6), A, C and D, and hence the stress and strain fields over the silica cladding region can be obtained. For different applied pressures in the hollow-core, the radial and azimuthal strains (ε_r and ε_θ), and the radial displacement ($u_r = r\varepsilon_\theta$) distribution for the entire cladding region are plotted in Fig. 6. The maximum strain happen near the wall

Optics EXPRESS

of hollow-core, and the maximum displacement happen near the outer edge of the cladding, and is about 1.25 nm for an applied pressure of 2 MPa.

Then, the refractive index of the silica cladding will be modified due to strain-optic effect. The changes of the three components of silica refractive index may be obtained through the strain distribution in the cross section of the HCF [31]:

$$\begin{cases} \Delta n_r = -\frac{1}{2} n_0^3 (p_{11}\varepsilon_r + p_{12}\varepsilon_\theta) \\ \Delta n_\theta = -\frac{1}{2} n_0^3 (p_{12}\varepsilon_r + p_{11}\varepsilon_\theta), \\ \Delta n_z = -\frac{1}{2} n_0^3 (p_{12}\varepsilon_r + p_{12}\varepsilon_\theta) \end{cases} \tag{7}$$

where $n_0 = 1.4446$ is the refractive index of silica under strain-free condition, and $p_{11} = 0.121$ and $p_{12} = 0.27$ are strain-optic tensor for bulk silica material. We calculated the changes of refractive index in silica cladding for 2 MPa, as shown in Fig. 7. It is shown that the change of the longitudinal component Δn_z is a constant while radial components reduce quickly with increasing radius. The maximum refractive index changes occur in the inner surface of the cladding with a value of $\sim 2.4 \times 10^{-5}$.

By importing the calculated results into Eq. (2), as shown in Figs. (6) and Figs. (7), we can estimate the structural deformation induced pressure sensitivity $S_{structure}$, and strain-optic effect induced pressure sensitivity S_{silica}. When the pressure level is increased to 2 MPa, the maximum deformation is about −1.25 nm, and $S_{structure}$ can be estimated to be −0.019 nm/MPa. Meanwhile, the maximum refractive index changes change of the mode index is $\sim 2.4 \times 10^{-5}$, corresponding to S_{silica} of ~0.022 nm/MPa. Noting that the $S_{structure}$ and S_{silica} are far less than the pressure-induced refractive index change of air within the hollow-core S_{air} (−3.398 nm/MPa). Furthermore, the pressure sensitivity $S_{structure}$ will counteract most strain-optic effect induced pressure sensitivity S_{silica}. This is an advantage of the proposed sensor, which greatly enhance its working pressure range.

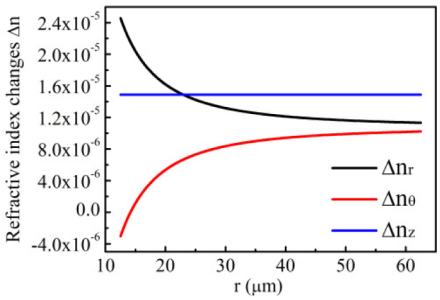

Fig. 7. The changes for individual refractive index component of silica cladding region for a 2 MPa pressure applied.

5. Temperature experiment

The influence of temperature on the proposed ARRG-based sensor has been investigated by placing the sensor (L = 5 mm) into an electrical oven and gradually increasing T from room temperature to 500°C, while monitoring the shift in a resonance transmission loss. Figure 8(a) shows the transmission spectrum evolution of the pressure sensor with respect to T, where a red shift is clearly observed with increasing T. The wavelength shift was recorded with respect to increasing T, and is given in Fig. 8 (b). Here, a linear relation is observed, with temperature coefficients of 26.97 pm/°C. The temperature response of the sensor is mainly

Optics EXPRESS

determined by the thermo-optical effect of the HCF. The temperature dependence of the proposed sensor can be expressed as:

$$\frac{\partial \lambda_m}{\partial T} = \frac{2dn_2}{m\sqrt{n_2^2 - n_1^2}} * \frac{dn_{silica}}{dT}, \tag{8}$$

where $dn_{silica}/dT = 1.1*10^{-5}/°C$ is the thermal-optical coefficient of silica [32]. Based on Eq. (8), the temperature sensitivity of the sensor at 1500 nm is estimated to be ~20.44 pm/°C, which is slightly lower than that obtained experimentally. In addition, the temperature cross-sensitivity can be calculated to be ~7.5 kPa/°C, which is much smaller than those of the sensor based on a π-phase-shifted FBG side-hole fiber (0.55 MPa/°C) [2] and based on a MZI in the dual core PCF (0.57 MPa/°C) [5].

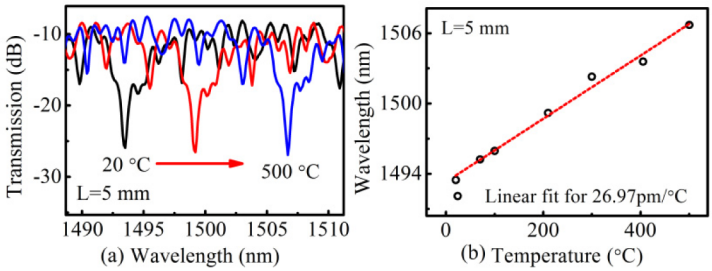

Fig. 8. (a) Transmission spectrum evolution of an ARRG-based pressure sensor (L = 5 mm) with respect to temperature. (b) Wavelength shifts of resonance dip with increasing temperature form 20°C to 500°C.

6. Conclusion

We have reported a new pressure sensor based on ARRG mechanism in an HCF. Resonant wavelengths result in sharp periodic lossy dips in the transmission spectrum of the device. The proposed sensor exhibits a high pressure sensitivity of 3.592 nm/MPa and a low temperature cross-sensitivity of 7.5 kPa/°C. Theoretical analysis indicates that the high pressure sensitivity originates from the pressure-induced refractive index change of air in the hollow-core, while the effects of pressure-induced structural change and index change of the silica cladding can be ignored. The proposed device employs novel sensing mechanism and exhibits simple and robust structure, which makes it an attractive candidate for highly sensitive gas pressure measurements in harsh environment and industrial applications.

Funding

National Natural Science Foundation of China (NSFC) (61425007, 61377090, 61575128, 61138006); Guangdong Provincial Department of Science and Technology (2014A030308007, 2014B050504010, 2015B010105007 and 2015A030313541), Science and Technology Innovation Commission of Shenzhen (ZDSYS20140430164957664, GJHZ20150313093755757, KQCX20140512172532195, JCYJ20160520163134575), and Pearl River Scholar Fellowships.